Geophysical Research Letters

RESEARCH LETTER
10.1029/2018GL080228

Key Points:
- Below the critical fraction, ~6%, particle-bearing ice behaves like pure ice and deforms by both grain boundary sliding and dislocation creep
- Above the critical fraction, ~6%, GBS creep is impeded in particle-bearing ice, as bands of particles separate ice clusters
- Icy masses on Mars, Ceres, and outer planet satellites could contain more ice than previously expected

Supporting Information:
- Supporting Information S1
- Figure S1
- Figure S2
- Figure S3
- Figure S4

Correspondence to:
C. Qi,
qichao@mail.iggcas.ac.cn

Citation:
Qi, C., Stern, L. A., Pathare, A., Durham, W. B., & Goldsby, D. L. (2018). Inhibition of grain boundary sliding in fine-grained ice by intergranular particles: Implications for planetary ice masses. *Geophysical Research Letters*, *45*, 12,757–12,765. https://doi.org/10.1029/2018GL080228

Received 30 AUG 2018
Accepted 10 NOV 2018
Accepted article online 16 NOV 2018
Published online 3 DEC 2018

Inhibition of Grain Boundary Sliding in Fine-Grained Ice by Intergranular Particles: Implications for Planetary Ice Masses

Chao Qi[1,2], Laura A. Stern[3], Asmin Pathare[4], William B. Durham[5], and David L. Goldsby[1]

[1]Department of Earth and Environmental Science, University of Pennsylvania, Philadelphia, PA, USA, [2]Now at Institute of Geology and Geophysics, Chinese Academy of Sciences, Beijing, China, [3]U.S. Geological Survey, Menlo Park, CA, USA, [4]Planetary Science Institute, Tucson, AZ, USA, [5]Department of Earth, Atmospheric, and Planetary Sciences, Massachusetts Institute of Technology, MA, USA

Abstract Ice in both terrestrial and planetary settings often contains rock particles. Here we present an experimental investigation of the influence of intergranular particles on the rheological behavior of ice. Experiments were performed on samples fabricated from 10-μm ice powders +1-μm graphite or 0.8-μm alumina particles and subjected to elevated confining pressures. A critical particle fraction, ~6%, was observed, below which samples behave like pure ice and deform by both grain boundary sliding (GBS) and dislocation creep, and above which GBS creep is impeded. Above this critical fraction, ice grains occur in particle-free clusters surrounded by bands of particles mixed with fine-grained ice, resulting in the impedance of GBS in the bands as well as sliding between the ice clusters. Our results imply that South Polar Layered Deposits and midlatitude lobate debris aprons on Mars must contain >94% ice and that the shallow subsurface of Ceres could contain >90% ice.

Plain Language Summary Ice on Mars, Ceres, and icy satellites often contains rock particles. The presence of particles in ice changes its flow behavior and thus is important for understanding the composition and evolution of planetary ice masses. Based on laboratory experiments on samples made of fine-grained ice and intergranular particles, we determined a critical quantity of particles, about 6% by volume, below which the ice-particle samples flow like pure ice, and above which, sliding between grains (so-called *grain boundary sliding*, or GBS) is impeded. The impedance of GBS by particles has not previously been observed. At planetary conditions, GBS is often the dominant flow mechanism for pure ice. Our result thus imply that the South Polar Layered Deposits and midlatitude lobate debris aprons on Mars must contain >94% ice and that the shallow subsurface of Ceres could contain more than 90% ice.

1. Introduction

Mixtures of insoluble rock particles and ice occur in both terrestrial and planetary settings, such as at the base of terrestrial ice sheets and glaciers (e.g., Drewry, 1986; Moore, 2014), in permafrost and polar ice caps on Mars (e.g., Kieffer, 1990; Squyres, 1989; Squyres & Carr, 1986), and on the surfaces and in the interiors of icy satellites (e.g., Anderson et al., 1996; Schubert et al., 2004; Showman & Malhotra, 1999). Knowledge of the flow behavior of ice-particle mixtures in these settings is critical for understanding the dynamics of terrestrial ice masses (e.g., Cohen, 2000; Dahl-Jensen et al., 1997), the dynamics of Martian glaciers (e.g., Fastook et al., 2014; Koutnik et al., 2013; Parsons et al., 2011), the viscous relaxation of impact craters throughout the solar system (e.g., Bland, 2013; Parmentier & Head, 1981; Pathare et al., 2005; Thomas & Schubert, 1988), and the subsurface structure of icy satellites (e.g., Friedson & Stevenson, 1983; Grindrod et al., 2008; Mueller & McKinnon, 1988). To describe the flow of ice-particle mixtures, rheological properties are often determined in well-controlled laboratory experiments and extrapolated to conditions found in nature using flow laws (Baker & Gerberich, 1979; Durham et al., 1992; Hooke et al., 1972; Mangold et al., 2002; Middleton et al., 2017; Yasui & Arakawa, 2008).

The flow law of ice for a given deformation mechanism can be described by a constitutive equation of the form

$$\dot{\varepsilon} = A\frac{\sigma^n}{d^p}\exp\left(-\frac{Q+PV^*}{RT}\right), \quad (1)$$

where $\dot{\varepsilon}$ is strain rate, A is a material parameter, σ is differential stress, n is the stress exponent, d is grain size, p is the grain-size exponent, Q is the activation energy for creep, P is the hydrostatic pressure, V^* is the activation volume for creep, R is the gas constant, and T is absolute temperature. Goldsby and Kohlstedt (2001) proposed a composite flow law that, for a wide range of planetary and terrestrial conditions of interest, can be simplified by expressing the total strain rate as

$$\dot{\varepsilon} = \dot{\varepsilon}_{\text{diff}} + \dot{\varepsilon}_{\text{GBS}} + \dot{\varepsilon}_{\text{disl}}. \quad (2)$$

Each term in this Goldsby-Kohlstedt composite flow law is a flow law of the form of equation (1). The subscript *diff* refers to the diffusion creep regime, the subscript *GBS* denotes grain boundary sliding (GBS) accommodated by basal dislocation slip with $n \approx 1.8$ and $p \approx 1.4$ (Goldsby & Kohlstedt, 1997; 2001). The subscript *disl* denotes dislocation creep with $n = 4$ and $p = 0$ (Durham et al., 1983; Kirby et al., 1987). Diffusion creep is not observed for the grain sizes and conditions of the experiments in this study. Thus, for the purposes of this paper, equation (2) can be further simplified to

$$\dot{\varepsilon} = \dot{\varepsilon}_{\text{GBS}} + \dot{\varepsilon}_{\text{disl}}. \quad (3)$$

Previous experimental studies on the rheological behavior of ice-particle mixtures have revealed that, below a critical particle fraction of ~10% to 15%, the strength of ice-particle mixtures is similar to that of pure ice, and above this critical fraction, strength increases with increasing particle fraction (Durham et al., 1992; Hooke et al., 1972; Middleton et al., 2017; Yasui & Arakawa, 2008). However, because these experiments were performed under various conditions, for example, at unconfined versus confined conditions, over a range of temperatures, and for larger versus smaller particles, it is difficult to synthesize the observations from different studies and determine the physical mechanisms that explain the influences of particles on rheological behavior. To date, the best description of the influence of particles on ice flow behavior is provided by the two experimental studies of Durham et al. (1992) and Middleton et al. (2017). In these studies, the strain rate of particle-bearing ice is described by an equation of the form

$$\dot{\varepsilon}_{\text{ice-particle}} = \exp(-b\phi)\dot{\varepsilon}_{\text{ice}}, \quad (4)$$

where b is a dimensionless parameter and ϕ is the volume fraction of particles. However, in spite of the good agreement between equation (4) and the experimental data in these studies, parameterizing the effect of particles on strain rate in terms of only the particle fraction (and not, e.g., the spatial distribution of particles, or their size) is likely an oversimplification.

Based on observations from previous studies and theoretical considerations, the influence that insoluble particles have on the rheological behavior of ice is a function of the following variables:

(1) *The distribution of particles*. Intragranular particles may impede the motion of lattice dislocations (Orowan hardening), while intergranular particles may increase the strength of grain boundary regions and impede GBS. Different distributions of particles may lead to different effects on the rheological behavior.
(2) *Particle size*. Intragranular particles of different sizes may induce different levels of distortion in the lattice of ice and impede the motion of dislocations by different amounts (Ebeling & Ashby, 1966). Intergranular particles of different sizes may have different effects on GBS and the strength of the grain boundary regions.
(3) *Mechanical strength of particles*. The strength of a matrix of particles may contribute to the strength of the ice-particle aggregate (Arenson et al., 2007; Goughnour, 1968; Moore, 2014).
(4) *Volume fraction of particles*. Previous experiments have shown that the strength of the ice-particle aggregate increases exponentially with increasing particle fraction (Durham et al., 1992; Middleton et al., 2017; Yasui & Arakawa, 2008).

In this study, we focus on the latter two variables, the mechanical strength of the particles and the fraction of particles, by carrying out laboratory deformation experiments on samples fabricated with intergranular, comparatively weak or strong particles, in both the dislocation creep and GBS creep regimes.

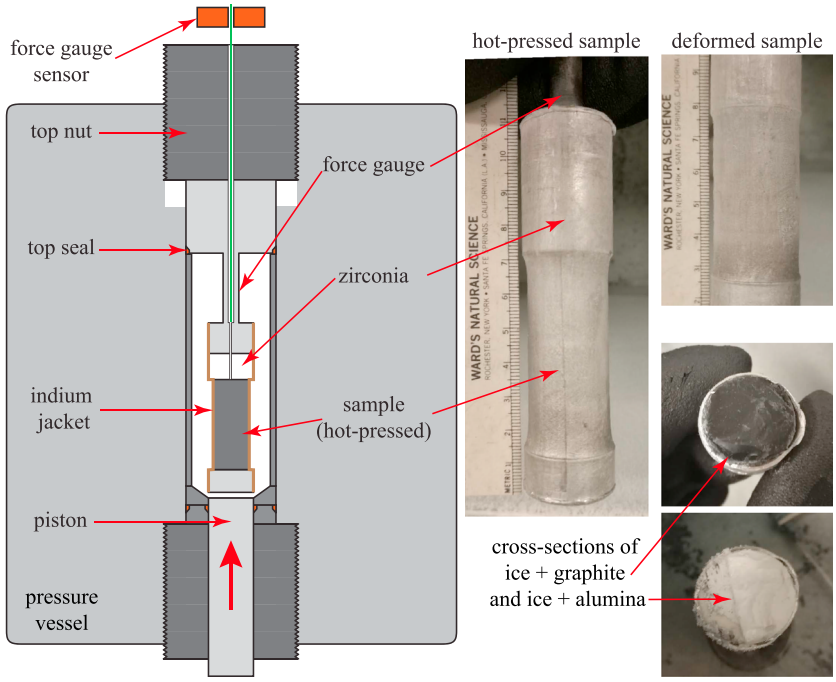

Figure 1. (left) Schematic of the pressure vessel with the deformation assembly inside. (right) Photos of hot-pressed and deformed samples. Details and dimensions of the pressure vessel can be found in Heard et al. (1990).

2. Methods

Samples were fabricated from mechanical mixtures of fine-grained powders of ice and nanopowders of graphite (1 μm in size) or alumina (α phase Al_2O_3, 0.3–0.8 μm in size). Both particles are approximately the same size relative to the ice grain size. The compressive strength of alumina is ~20 times that of graphite. Details of the sample preparation are given in the supporting information. Experiments were carried out in axial compression at $T = 236$ K and a confining pressure of $P = 20$ MPa in a cryogenic, gas-medium apparatus (Durham et al., 1983) illustrated in Figure 1. Prior to deformation, each sample was "hot-pressed" at the experimental temperature and pressure for about 2–3 hr, so that the sample became fully dense. After "hot-pressing", each sample was taken out of the pressure vessel and its length and diameter measured. The sample was then repressurized and allowed to equilibrate at the deformation temperature and pressure for about 1 hr. Deformation experiments were performed at constant displacement rate (yielding a nominally constant strain rate), which was stepped multiple times during an experiment, yielding strain rates in the range $10^{-6.5}$ to $10^{-3.5}$ s^{-1}. Each strain rate was maintained until a peak in the load (stress) was reached, typically after an axial-strain increment of ~0.02. The duration of each strain-rate segment was kept as short as possible to help maintain a roughly constant microstructure. Strain rates were stepped sequentially from low to high values, and experiments were terminated after completing the fastest strain-rate step. The raw mechanical data were processed to obtain strain, strain rate, and stress, as detailed in the supporting information. After each run, the deformed sample was photographed and stored in liquid nitrogen for subsequent analysis of particle distribution and grain-scale characteristics by cryogenic scanning electron microscopy (cryo-SEM).

3. Results

3.1. Microstructural Data

The cryo-SEM micrographs in Figures 2a–2c reveal the distribution of graphite particles in the ice after deformation. In the micrographs, an individual graphite particle is below the resolution of the microscope, but clumps of particles can be easily seen (as indicated by the red arrows). The ice "grains" are actually polycrystalline clusters of smaller grains, with cluster sizes in the range of 30 to 80 μm. These ice clusters are formed in the water droplets frozen in liquid nitrogen during the spraying process (see the supporting information). Each cluster of ice grains is separated from its neighbors by graphite particles that are likely mixed with fine-grained ice. Within each ice cluster, no graphite clumps are observed, and ice-ice grain boundaries are widely observed

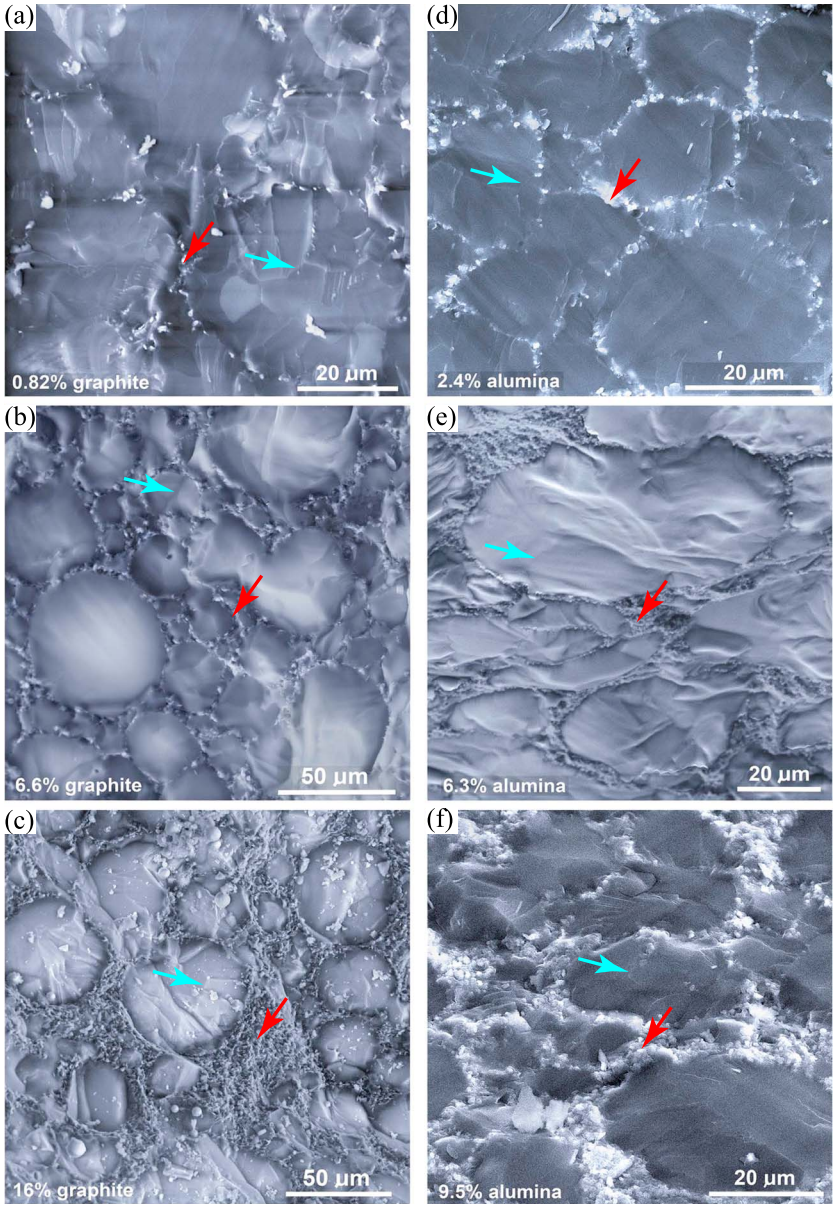

Figure 2. Cryogenic scanning electron microscopy images comparing three ice + graphite samples (a–c) with three ice + alumina samples of comparable particle fraction (d–f). Particles are generally the small/bright pixels; red arrows mark several examples of regions containing particles. The large rounded *grains* are clusters of fine-grained ice, with blue arrows pointing to examples of ice-ice boundaries within the clusters (see also supporting information Figure S2). Panels (a) through (f) compare samples containing 0.82% graphite (PIL111), 6.6% graphite (PIL99), 16% graphite (PIL115), 2.4% alumina (PIL125), 6.3% alumina (PIL120), and 9.5% alumina (PIL124), respectively. Larger regional views of the samples in (c) and (f) are compared in supporting information Figure S3. With increasing particle fraction, both the graphite-bearing and alumina-bearing samples show progressive development of bands of particles surrounding the ice clusters.

(blue arrows). The grain size of the ice grains in the clusters is about 10 μm, which is estimated based on a line intercept method for a section shown in supporting information Figure S2. In the sample with 0.82% graphite (PIL111, Figure 2a), graphite particles lie between the clusters of ice grains. In the sample with 6.6% graphite (PIL99, Figure 2b), graphite particles similarly lie between clusters of ice grains, and a narrow band of graphite, or graphite mixed with ice, forms. In the sample with 16% graphite (PIL115, Figure 2c), graphite particles form bands that completely separate ice clusters. The exposed surfaces of the graphite bands, created by cleaving the samples for SEM analysis, are rough in character. Tiny ice grains likely exist in the bands of graphite particles, as the bands are mottled with brighter (graphite) and darker (ice) colors.

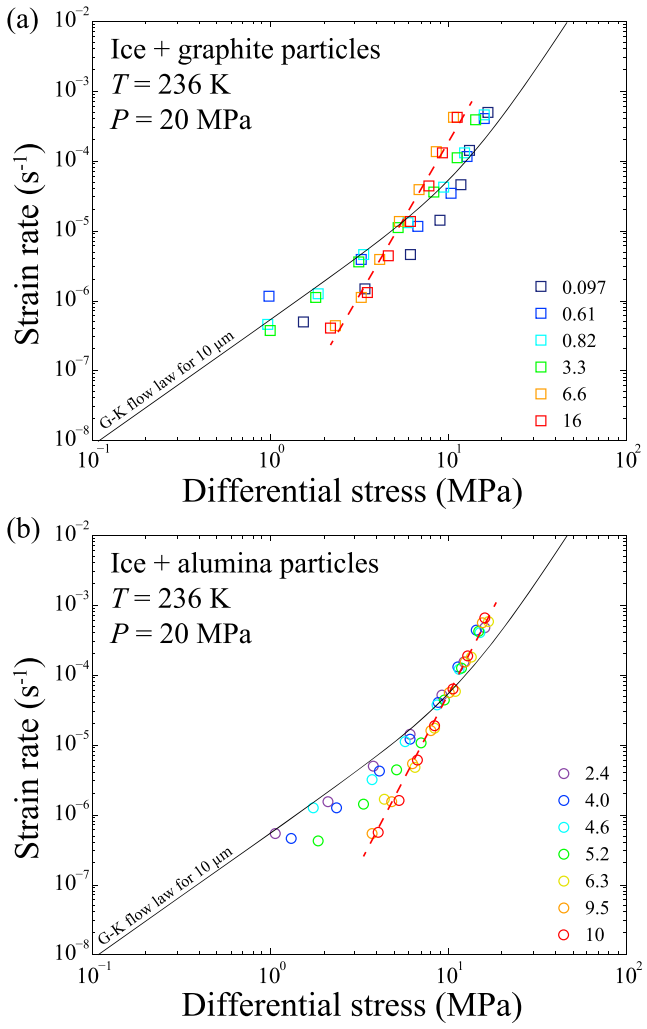

Figure 3. Plot of strain rate versus stress on logarithmic scales for samples of (a) ice + graphite particles and (b) ice + alumina particles. The black curve represents the flow law for pure ice for a grain size of 10 μm (Goldsby & Kohlstedt, 2001). The volume fraction of particles for each sample is shown as a percentage in the bottom right of each panel. In panel (a), from colder to warmer colors of the markers are samples PIL116, PIL114, PIL111, PIL112, PIL99, and PIL115. The dashed red line is a linear fit of the data from experiments on high-fraction samples (PIL99 and PIL115) with a slope of 4.4 ± 0.2. In panel (b), from colder to warmer colors of markers are samples PIL125, PIL122, PIL119, PIL121, PIL120, PIL124, and PIL123. The dashed red line is a linear fit of the data from experiments on high-particle-fraction samples (PIL120, PIL124, and PIL123) with a slope of 4.8 ± 0.1.

The distribution of particles in alumina-bearing samples is very similar to that of the graphite-bearing samples. Figure 2d shows that the alumina particles are distributed between polycrystalline clusters of ice grains, with ice cluster sizes in the range of 20 to 80 μm. Within each cluster, no alumina is observed, while ice-ice grain boundaries are widely observed (blue arrows in Figure 2 and supporting information Figure S2). The average grain size of the ice is about 10 μm. Ice clusters in alumina-bearing samples are slightly more elongated than those in graphite-bearing samples, as illustrated in supporting information Figure S3. Alumina particles assemble as thin bands along the boundaries between the ice clusters and lie at three- and four-grain junctions between clusters. The exposed surfaces in the alumina bands are very rough in appearance, as in the graphite-bearing samples.

3.2. Mechanical Data

During each experiment, multiple strain-rate steps were performed. Four stress-strain curves are presented in supporting information Figure S4. For each strain-rate step, the peak stress was determined. Thus, each experiment yielded six or seven data points. The mechanical data for all samples are summarized in supporting information Table S1.

Samples of ice + graphite deformed at strain rates of $10^{-6.5} \leq \dot{\varepsilon} \leq 10^{-3.5}$ s^{-1} show strengths of $1 \leq \sigma \leq 17$ MPa, as illustrated in the logarithmic plot of $\dot{\varepsilon}$ versus σ in Figure 3a. For samples with less than 4% graphite, all data points lie near the curve calculated using the Goldsby-Kohlstedt composite flow law (equation (3)) for pure ice with a grain size of 10 μm. At higher stresses (σ >10 MPa), the data points at a given stress lie at higher strain rates than predicted from the composite law. More importantly, no correlation is observed between the sample strength and the particle fraction for a particle fraction <4%. For samples with >6% graphite, instead of following the two-mechanism trend of the composite flow law, all data points lie on a straight line. A linear fit to the data reveals a slope of 4.4 ± 0.2 (dashed red line in Figure 3a). At $\dot{\varepsilon} \leq 10^{-6}$ s^{-1}, samples with higher fractions of graphite (ϕ >6%) are stronger than samples with lower fractions of graphite (ϕ <4%). At $\dot{\varepsilon} \geq 10^{-5}$ s^{-1}, samples with higher fractions of graphite (ϕ >6%) are weaker than samples with lower fractions of graphite (ϕ <4%).

Samples of ice + alumina deformed at strain rates of $10^{-6.5} \leq \dot{\varepsilon} \leq 10^{-3.5}$ s^{-1} show strengths of $1 \leq \sigma \leq 16$ MPa, as illustrated in the logarithmic plot of $\dot{\varepsilon}$ versus σ in Figure 3b. The variation of the mechanical behavior with particle fraction for these samples is very similar to that for the graphite-bearing ice samples described above. For samples with <6% alumina, all data points lie near the curve calculated from the composite flow law for pure ice for a grain size of 10 μm. At higher stresses (σ >10 MPa), the data points lie to the left of the composite law curve. For samples with <6% alumina, at stresses <10 MPa, strength increases with increasing particle fraction, except for the sample with 4.6% alumina (PIL119). For samples with >6% alumina, instead of following the curvature of the composite flow law, all data points lie on a straight line. A linear fit to the data reveals a slope of 4.8 ± 0.1 (dashed red line in Figure 3b). At all strain rates, samples with higher fractions of alumina (ϕ >6%) have the same strength as or are stronger than samples with lower fractions of alumina (ϕ <6%).

4. Discussion

4.1. The Influence of Rock Fraction

As illustrated in Figures 3 and 4a, the particle-bearing ice samples exhibit two distinct types of rheological behaviors determined by a critical particle fraction $\phi_c \approx 6\%$.

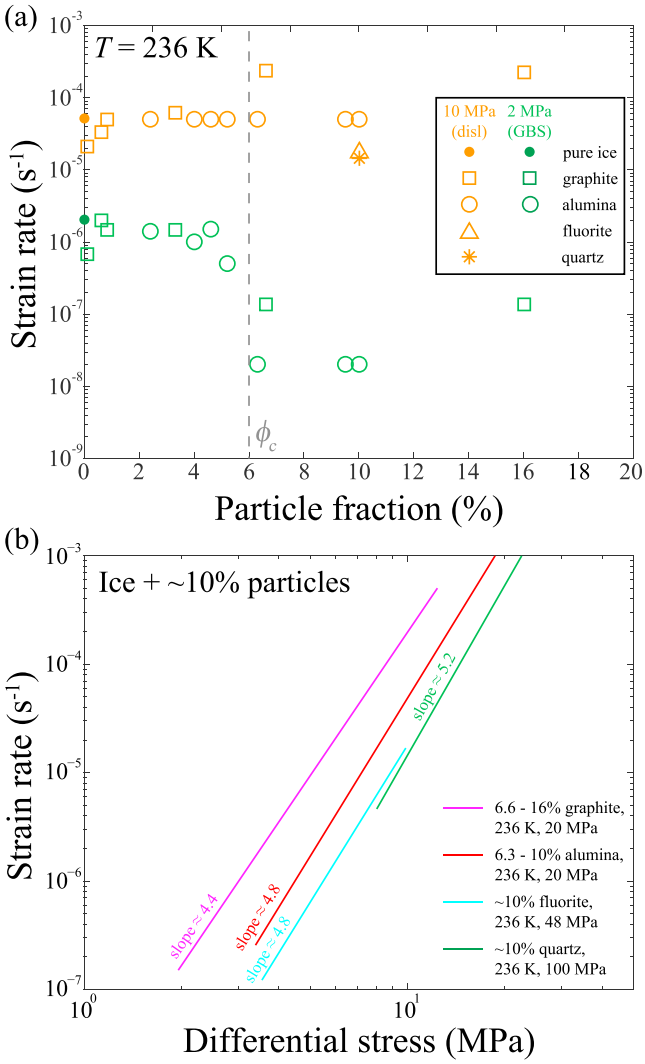

Figure 4. Comparison for data of this study, Durham et al. (1992) and Middleton et al. (2017). Data for ice + fluorite (Middleton et al., 2017) were extrapolated to T = 236 K, using an activation energy of Q = 60 kJ/mol (Goldsby & Kohlstedt, 2001). Data for ice + quartz (Durham et al., 1992) were extrapolated to T = 236 K, using values of activation energy published in Durham et al. (1992). (a) Plot of strain rate versus particle fraction. Strain rates corresponding to differential stresses of 2 MPa (green) and 10 MPa (orange) are presented for pure ice, ice + graphite, alumina, fluorite, and quartz particles. At 2 MPa, the dominant deformation mechanism is grain boundary sliding, whereas at 10 MPa, dislocation creep dominates. Data for pure ice were calculated using equation (3) with d = 10 μm. Data for ice + graphite and ice + alumina were interpolated or extrapolated from our results. Data for ice + fluorite and ice + quartz were not extrapolated to 2 MPa, as these samples were deformed via dislocation creep. (b) Plot of strain rate versus stress on logarithmic scales. The lines are linear fits of the data from our experiments and those of Middleton et al. (2017) and Durham et al. (1992).

(i) For $\phi < \phi_c$, particle-bearing samples deform in the same manner as pure ice; that is, the rheological behavior of the aggregate is characterized by dislocation creep with $n \approx 4$ at high stresses/strain rates and GBS creep with $n \approx 1.8$ at low stresses/strain rates. No obvious correlation between sample strength and particle fraction is found for $\phi < \phi_c$. At higher stresses (σ >10 MPa), particle-bearing samples are slightly weaker than pure ice, which may be due to the fact that these data points were obtained at relatively high strains (~0.1), such that deformation has weakened the samples, for example, due to the development of a crystallographic preferred orientation (e.g., Hansen et al., 2016). As suggested by the microstructures shown in Figure 2, at $\phi < \phi_c$, only a small number of ice grain boundaries are replaced by ice-particle phase boundaries. The existence of a large fraction of ice-ice grain boundaries allows GBS to occur readily at low stresses. Assuming the ice grain size in samples of ice with particles remains roughly constant during an

experiment, due to grain boundary pinning effects (Smith, 1948) and perhaps dynamic recrystallization due to subgrain rotation, the rheological behavior of particle-bearing ice at $\phi < \phi_c$ can be approximated by using the simplified pure-ice flow law:

$$\dot{\varepsilon}_{\text{ice-particle}}(\phi < \phi_c) \approx \dot{\varepsilon}_{\text{ice}} = \dot{\varepsilon}_{\text{disl}} + \dot{\varepsilon}_{\text{GBS}}. \quad (5)$$

(ii) For $\phi > \phi_c$, particle-bearing ice samples deform by a single deformation mechanism characterized by an effective stress exponent $n_{\text{eff}} > 4$. As suggested by the microstructures illustrated in Figure 2, for $\phi > \phi_c$, the clusters of ice grains are bounded by complex regions of mixed particles and ice (see Figures 2c and 2f), and ice-ice grain boundaries may only exist within the polycrystalline ice clusters. The existence of particles in the regions between ice clusters may prevent GBS between ice grains and ice clusters. Thus, with GBS impeded, the sample deforms by dislocation creep. The high value of the effective stress exponent is thus the result of dislocation creep of the ice. The rheological behavior of particle-bearing ice samples at $\phi > \phi_c$ can be described as

$$\dot{\varepsilon}_{\text{ice-particle}}(\phi > \phi_c) \approx F\dot{\varepsilon}_{\text{disl}}, \quad (6)$$

where F is a factor reflecting the strength and fraction of the particles. At low strain rates ($\dot{\varepsilon} \leq 10^{-6}$ s^{-1}), $F \approx 3$ for ice + graphite and $F \approx 1$ for ice + alumina.

4.2. The Influence of Particle Strength

For $\phi < \phi_c$, both ice + graphite and ice + alumina samples exhibit the same rheological behavior, which is similar to that of pure ice. However, for $\phi > \phi_c$, ice + alumina samples are 1.3 to 1.5 times stronger than ice + graphite samples throughout the full range of investigated strain rates, as illustrated in Figure 4. Previous studies have shown that the strength of ice-particle aggregates increases rapidly and becomes similar to that of dry sand when the sand fraction exceeds 56% (Durham et al., 1992). At such high fractions, the increase of the strength of the aggregate is attributed to the strength of an interconnected, stress-supporting matrix (Arenson et al., 2007; Goughnour, 1968; Moore, 2014). In our experiments, when particles are located in bands that separate clusters of ice grains, deformation must occur within the aggregates of particles, and thus, the strength of the particle matrix may become important. The strength of an aggregate of alumina particles is higher than that of graphite particles (Paterson & Edmond, 1972). Our observations demonstrate that the strength of the aggregate of particles has a modest effect on the rheological behavior of the ice-particle samples for $\phi > \phi_c$ (6%).

4.3. Comparisons With Previous Studies

Durham et al. (1992) reported results from deformation experiments on ice containing three types of particles, with particle fractions in the range of 0.001 to 0.56. An exponential increase in the strength of particle-bearing samples with increasing particle fraction was observed in their study. Since variations in ice grain size, particle size, and particle distribution existed in the samples of Durham et al. (1992), we can only make a few direct comparisons with the results of our study. Agreement between the observations of Durham et al. (1992) and this study is summarized as follows: (1) Samples of ice containing 0.1% of 20-μm silicon carbide particles in the Durham et al. (1992) study show a similar strength to that of pure ice. (2) A comparison between data from experiments on samples of similar particle fractions (~10%), illustrated in Figure 4, reveals that the values of the effective stress exponents are similar for ice + 100-μm quartz particles and for our ice + alumina samples but that the ice + quartz samples are ~1.2 times stronger than our ice + alumina samples.

Recently, Middleton et al. (2017) reported results from deformation experiments on ice with a grain size of 185 ± 50 μm containing intergranular fluorite (CaF_2) particles 100–200 μm in size under a confining pressure of 48 MPa at temperatures of 263 and 253 K. The data from these experiments were analyzed in a similar manner as ours were and included data from both the dislocation creep and GBS creep regimes, thus allowing for a relevant comparison with our data. Middleton et al. (2017) observed an effective stress exponent with values between 4 and 5 in experiments on samples bearing 10%, 25%, and 50% particles. Samples with 10% and 25% particles exhibit similar strength, while samples with 50% particles were stronger than the other two groups. Observations of Middleton et al. (2017) and from this study are in good agreement and can be synthesized as follows: (1) GBS creep is impeded for samples with $\phi > 6\%$ in this study and in Middleton et al. (2017), and (2) a comparison between data from experiments on samples of similar particle fractions (Figure 4b) reveals that the value of the effective stress exponent is the same for ice + fluorite samples and for ice + alumina samples but that the strength of ice + fluorite samples is higher than that of ice + alumina samples, and similar to

that of ice + quartz samples in the Durham et al. (1992) study. These differences in strength between samples containing different particles may be due to the difference in the relative particle size. The particle size is ~0.1 times the ice grain size in our study versus ~1 times the ice grain size in Middleton et al. (2017).

4.4. Implications for Planetary Ice Masses

The inhibition of GBS creep at relatively low (>6%) intergranular particle fractions has important implications for the composition and evolution of ice masses on Mars, Ceres, and outer planet satellites. For example, consider the Martian South Polar Layered Deposits (SPLDs), which based on the crater counts of Koutnik et al. (2002) exhibit a relatively young crater retention surface age of 30–100 Ma. Pathare et al. (2005) showed that the ubiquitous shallowness of SPLD craters is most consistent with modification primarily via viscous relaxation over these timescales—provided that GBS creep occurs within the SPLD. That is because, at typical SPLD subsurface conditions ($T = 175$ K, driving stress $\sigma = 100$ kPa, ice grain size of $d = 1$ mm), the effective viscosity of ice only undergoing dislocation creep is approximately 3 orders of magnitude greater than ice undergoing GBS creep (which as discussed in the appendix of Pathare et al., 2005, applies for a wide range of plausible variations in rheological parameters).

Therefore, our new laboratory results suggest that the SPLD must be composed of >94% ice in order for SPLD craters to exhibit modification via viscous relaxation creep over multimillion year timescales as indicated by Pathare et al. (2005). This may seem somewhat counterintuitive, given that the namesake layering of the PLD is due to the presence of dust, but shallow radar measurements indicate that the Martian North PLD consists of >95% pure ice (Grima et al., 2009). What is perhaps more unexpected is that Martian lobate debris aprons at midlatitudes, which exhibit far more evidence of recent glacial flow over the past 100 Myr than the PLD (e.g., Parsons et al., 2011), must also contain less than 6% dust despite flowing beneath a protective debris cover.

Our results also have important implications for Ceres and outer planet satellites. Based on the absence of viscous relaxation over billion-year timescales, Bland et al. (2016) concluded that the shallow subsurface of Ceres contains no more than 30–40% ice by volume. However, this analysis assumed that GBS creep was affected by dust in the same manner as dislocation creep (see Methods section of Bland et al., 2016). Inhibition of GBS creep by >6% dust would allow ice fractions greater than 90% in Ceres' shallow subsurface, which is potentially more consistent with the presence of the recently flowing Ahuna Mons ice mass on the surface (Sori et al., 2017). Similarly, our work may also help constrain the composition of outer planet satellites exhibiting crater relaxation, such as Ganymede and Callisto (Dombard & McKinnon, 2006) and Enceladus (Kirchoff & Schenk, 2009).

5. Conclusions

- A rheologically critical particle fraction, ϕ_c, was observed for both graphite- and alumina-bearing samples. Below ϕ_c, particle-bearing samples deform in the same manner as pure ice, exhibiting both GBS and dislocation creep behaviors. Above ϕ_c, particle-bearing samples deform by a single deformation mechanism with a value of the stress exponent >4, dislocation creep. That is, GBS creep is impeded.
- Both graphite and alumina particles are distributed in the same manner in the samples. Below ϕ_c, particles are found in clumps between clusters of ice grains. Above ϕ_c, particles are found in interconnected particle-rich bands that surround particle-free clusters of ice grains. This microstructural observation suggests that the impedance of GBS creep is caused by the presence of particles in the boundary regions between ice clusters.
- Above ϕ_c, ice + alumina samples are 1.3 to 1.5 times stronger at a given strain rate than ice + graphite samples. This observation suggests that the strength of the particle-bearing samples is higher for stronger particles.
- The inhibition of GBS creep by intergranular particles means that if such particles are homogeneously distributed within icy masses undergoing glacial flow or viscous relaxation at low stresses on Mars, Ceres, and outer planet satellites, then such flowing or relaxing ice masses are likely composed of >94% ice.

Acknowledgments
We thank T. Werts and J. Anderson (University of Pennsylvania) for their help with experiments and J. Jang and C. Morrow (both at the USGS) plus two anonymous reviewers for very helpful reviews of the manuscript. This work was supported by NASA Solar System Workings program (NNX15AM69G). All experimental data are presented in supporting information Table S1.

References

Anderson, J. D., Lau, E. L., Sjogren, W. L., Schubert, G., & Moore, W. B. (1996). Gravitational constraints on the internal structure of Ganymede. *Nature*, *384*(6609), 541–543.

Arenson, L. U., Springman, S. M., & Sego, D. C. (2007). The rheology of frozen soils. *Applied Rheology*, *17*(1), 12147–1–12147-14.

Baker, R. W., & Gerberich, W. W. (1979). The effect of crystal size and dispersed-solid inclusions on the activation energy for creep of ice. *Journal of Glaciology*, *24*(90), 179–194.

Bland, M. T. (2013). Predicted crater morphologies on Ceres: Probing internal structure and evolution. *Icarus*, *226*(1), 510–521.
Bland, M. T., Raymond, C. A., Schenk, P. M., Fu, R. R., Kneissl, T., Pasckert, J. H., et al. (2016). Composition and structure of the shallow subsurface of Ceres revealed by crater morphology. *Nature Geoscience*, *9*(7), 538–542.
Cohen, D. (2000). Rheology of ice at the bed of Engabreen, Norway. *Journal of Glaciology*, *46*(155), 611–621.
Dahl-Jensen, D., Thorsteinsson, T., Alley, R. B., & Shoji, H. (1997). Flow properties of the ice from the Greenland ice core project ice core: The reason for folds? *Journal of Geophysical Research*, *102*(C12), 26,831–26,840.
Dombard, A. J., & McKinnon, W. B. (2006). Elastoviscoplastic relaxation of impact crater topography with application to Ganymede and Callisto. *Journal of Geophysical Research*, *111*, E01001. https://doi.org/10.1029/2005JE002445
Drewry, D. (1986). Glacial geologic processes, Edward Arnold Baltimore.
Durham, W. B., Heard, H. C., & Kirby, S. H. (1983). Experimental deformation of polycrystalline H_2O ice at high pressure and low temperature: Preliminary results. *Journal of Geophysical Research*, *88*(S01), B377–B392. https://doi.org/10.1029/JB088iS01p0B377
Durham, W. B., Kirby, S. H., & Stern, L. A. (1992). Effects of dispersed particulates on the rheology of water ice at planetary conditions. *Journal of Geophysical Research*, *97*(E12), 20,883–20,897. https://doi.org/10.1029/92JE02326
Ebeling, R., & Ashby, M. F. (1966). Dispersion hardening of copper single crystals. *Philosophical Magazine*, *13*(124), 805–834.
Fastook, J. L., Head, J. W., & Marchant, D. R. (2014). Formation of lobate debris aprons on Mars: Assessment of regional ice sheet collapse and debris-cover armoring. *Icarus*, *228*, 54–63.
Friedson, A. J., & Stevenson, D. J. (1983). Viscosity of rock-ice mixtures and applications to the evolution of icy satellites. *Icarus*, *56*(1), 1–14.
Goldsby, D. L., & Kohlstedt, D. L. (1997). Grain boundary sliding in fine-grained Ice I. *Scripta Materialia*, *37*(9), 1399–1406.
Goldsby, D. L., & Kohlstedt, D. L. (2001). Superplastic deformation of ice: Experimental observations. *Journal of Geophysical Research*, *106*(B6), 11,017–11,030. https://doi.org/10.1029/2000JB900336
Goughnour, R. R., & Andersland, O. (1968). Mechanical properties of a sand-ice system. *Journal of the Soil Mechanics American Society of Civil Engineers American Society*, *94*, 923–950.
Grima, C., Kofman, W., Mouginot, J., Phillips, R. J., Hérique, A., Biccari, D., et al. (2009). North polar deposits of Mars: Extreme purity of the water ice. *Geophysical Research Letters*, *36*, L03203. https://doi.org/10.1029/2008GL036326
Grindrod, P. M., Fortes, A. D., Nimmo, F., Feltham, D. L., Brodholt, J. P., & Vočadlo, L. (2008). The long-term stability of a possible aqueous ammonium sulfate ocean inside Titan. *Icarus*, *197*(1), 137–151.
Hansen, L. N., Warren, J. M., Zimmerman, M. E., & Kohlstedt, D. L. (2016). Viscous anisotropy of textured olivine aggregates, Part 1: Measurement of the magnitude and evolution of anisotropy. *Earth and Planetary Science Letters*, *445*, 92–103.
Heard, H. C., Durham, W. B., Boro, C. O., & Kirby, S. H. (1990). A triaxial deformation apparatus for service at $77 \leq T \leq 273$ K. In A. G. Duba (Ed.), *The brittle-ductile transition in rocks, Geophysical Monograph Series* (Vol. 56, pp. 225–228). Washington, D. C.: AGU.
Hooke, R. L., Dahlin, B. B., & Kauper, M. T. (1972). Creep of ice containing dispersed fine sand. *Journal of Glaciology*, *11*(63), 327–336.
Kieffer, H. H. (1990). H_2O, grain size and the amount of dust in Mars' residual north polar cap. *Journal of Geophysical Research*, *95*(B2), 1481–1493.
Kirby, S. H., Durham, W. B., Beeman, M. L., Heard, H. C., & Daley, M. A. (1987). Inelastic properties of ice Ih at low temperatures and high pressures. *Journal de Physique Colloques*, *48*(C1), C1–227.
Kirchoff, M. R., & Schenk, P. (2009). Crater modification and geologic activity in Enceladus' heavily cratered plains: Evidence from the impact crater distribution. *Icarus*, *202*(2), 656–668.
Koutnik, M., Byrne, S., & Murray, B. (2002). South Polar Layered Deposits of Mars: The cratering record. *Journal of Geophysical Research*, *107*(E11), 5100.
Koutnik, M. R., Waddington, E. D., Winebrenner, D. P., & Pathare, A. V. (2013). Response timescales for martian ice masses and implications for ice flow on Mars. *Icarus*, *225*(2), 949–959.
Mangold, N., Allemand, P., Duval, P., Geraud, Y., & Thomas, P. (2002). Experimental and theoretical deformation of ice–rock mixtures: Implications on rheology and ice content of Martian permafrost. *Planetary and Space Science*, *50*(4), 385–401.
Middleton, C. A., Grindrod, P. M., & Sammonds, P. R. (2017). The effect of rock particles and D_2O replacement on the flow behaviour of ice. *Philosophical Transactions of the Royal Society A*, *375*(2086), 20150349.
Moore, P. L. (2014). Deformation of debris-ice mixtures. *Reviews of Geophysics*, *52*, 435–467.
Mueller, S., & McKinnon, W. B. (1988). Three-layered models of Ganymede and Callisto: Compositions, structures, and aspects of evolution. *Icarus*, *76*(3), 437–464.
Parmentier, E. M., & Head, J. W. (1981). Viscous relaxation of impact craters on icy planetary surfaces: Determination of viscosity variation with depth. *Icarus*, *47*(1), 100–111.
Parsons, R. A., Nimmo, F., & Miyamoto, H. (2011). Constraints on martian lobate debris apron evolution and rheology from numerical modeling of ice flow. *Icarus*, *214*(1), 246–257.
Paterson, M. S., & Edmond, J. M. (1972). Deformation of graphite at high pressures. *Carbon*, *10*(1), 29–34.
Pathare, A. V., Paige, D. A., & Turtle, E. (2005). Viscous relaxation of craters within the Martian south polar layered deposits. *Icarus*, *174*(2), 396–418.
Schubert, G., Anderson, J. D., Spohn, T., & McKinnon, W. B. (2004). Interior composition, structure and dynamics of the Galilean satellites. *Jupiter: The planet, satellites and magnetosphere*, *1*, 281–306.
Showman, A. P., & Malhotra, R. (1999). The Galilean satellites. *Science*, *286*(5437), 77–84.
Smith, C. S. (1948). Zener pinning. *Transactions of the Metallurgical Society of AIME*, *175*, 15–51.
Sori, M. M., Byrne, S., Bland, M. T., Bramson, A. M., Ermakov, A. I., Hamilton, C. W., et al. (2017). The vanishing cryovolcanoes of Ceres. *Geophysical Research Letters*, *44*, 1243–1250. https://doi.org/10.1002/2016GL072319
Squyres, S. W. (1989). Urey prize lecture: Water on Mars. *Icarus*, *79*(2), 229–288.
Squyres, S. W., & Carr, M. H. (1986). Geomorphic evidence for the distribution of ground ice on Mars. *Science*, *231*(4735), 249–252.
Thomas, P. J., & Schubert, G. (1988). Power law rheology of ice and the relaxation style and retention of craters on Ganymede. *Journal of Geophysical Research*, *93*(B11), 13,755–13,762.
Yasui, M., & Arakawa, M. (2008). Experimental study on the rate dependent strength of ice-silica mixture with silica volume fractions up to 0.63. *Geophysical Research Letters*, *35*, L12206. https://doi.org/10.1029/2008GL033787